Electron and ion kinetic effects in the saturation of a driven ion acoustic wave

C. Riconda[a)]
*Centre de Physique Théorique, UMR CNRS 7644, École Polytechnique, 91128 Palaiseau Cedex, France
and Centre des Lasers Intenses et Applications, UMR CNRS 5107, Université Bordeaux 1,
Commissariat à l'Energie Atomique (CEA), Université Bordeaux 1, 33405 Talence Cedex, France*

A. Heron, D. Pesme, and S. Huller
Centre de Physique Théorique, UMR CNRS 7644, École Polytechnique, 91128 Palaiseau Cedex, France

V. T. Tikhonchuk
*Centre des Lasers Intenses et Applications, UMR CNRS 5107, Université Bordeaux 1, Commissariat
à l'Energie Atomique (CEA), Université Bordeaux 1, 33405 Talence Cedex, France*

F. Detering
Centre de Physique Théorique, UMR CNRS 7644, École Polytechnique, 91128 Palaiseau Cedex, France

The role of ion and electron kinetic effects is investigated in the context of the nonlinear saturation of a driven ion acoustic wave (IAW) and its parametric decay into subharmonics. The simulations are carried out with a full–particle-in-cell (PIC) code, in which both ions and electrons are treated kinetically. The full-PIC results are compared with those obtained from a hybrid-PIC code (kinetic ions and Boltzmann electrons). It is found that the largest differences between the two kinds of simulations take place when the IAW is driven above the ion wave-breaking limit. In such a case of a strong drive, the hybrid-PIC simulations lead to a Berstein-Greene-Kruskal-like nonlinear IAW of a large amplitude, while in the full-PIC the IAW amplitude decays to a small level after a transient stage. The electron velocity distribution function is significantly flattened in the domain of small electron velocities. As a result the nonlinear frequency shift due to the electron kinetic effects compensates partly the nonlinear frequency shift due to the ion kinetic effects, allowing then for the parametric decay of the driven IAW into subharmonics. These observations lead to the conclusion that electron kinetic effects become important whenever the nonlinear effects come into play.
© *2005 American Institute of Physics.* [DOI: 10.1063/1.2132272]

I. INTRODUCTION

Understanding of the nonlinear ion acoustic wave (IAW) behavior is a fundamental problem of great interest, with an important incidence in the context of laser-plasma interaction. In particular, the IAW nonlinearities are considered to be responsible for the fact that the stimulated Brillouin scattering (SBS) of the laser light in present day experiments develops at a much lower level than predicted by the linear theory. However, the extrapolation of this result to laser fusion-relevant conditions, leading to the conclusion that SBS will stay at a low level, remains highly questionable. An appropriate understanding of the saturation mechanism is therefore of high importance for predictive modeling. Various nonlinear mechanisms have been invoked to explain the IAW saturation, including fluid-type effects such as the harmonics and/or the subharmonics generation, presence of long-wavelength density fluctuations, laser momentum deposition, and ion kinetic effects.[1–14]

It is now widely accepted that ion kinetic effects play an important role even for the IAW amplitudes below the wave-breaking limit,[15] at which the ion distribution function is strongly modified. Weak kinetic effects have been studied analytically in the limit of a modification of the distribution function around the IAW phase velocity only. Such a modification of the ion distribution function leads to the suppression of the Landau damping, on one hand, and to a nonlinear frequency shift, on the other hand.[16,17] The existence of a nonlinear frequency shift results, in turn, in a local detuning of the three-wave resonance condition, and such a nonlinear detuning has been invoked to explain the saturation of the SBS reflectivity.[3,13,18–22] The parametric decay of the driven IAW into subharmonics, a process also called the "two-ion decay," has been suggested as another mechanism to explain the saturation of the SBS reflectivity. By this process the SBS-driven IAW energy is transferred to long-wavelength IAWs (subharmonics), which cannot be resonantly coupled to SBS.[5] The generation of subharmonics of the SBS-driven IAW has been observed for the first time in two-dimensional (2D) simulations with the hybrid particle-in-cell (PIC) code BZOHAR (kinetic ions and Boltzmann electrons).[6] It has then been observed in one-dimensional (1D) simulations using similar hybrid codes.[12,13] Experimental evidence of the IAW parametric decay was reported recently in Refs. 23 and 24.

In this paper, we discuss in detail the saturation of a driven IAW, addressing, in particular, the connection between the parametric decay and kinetic effects.[25] To do so, we consider the simulation results obtained from two 1D

[a)]Electronic mail: riconda@celia.u-bordeaux1.fr

codes: (i) a "full-PIC" code, in which both particle species are kinetic, and (ii) a "hybrid-PIC" code, in which the ions are kinetic and the electrons are described by the Boltzmann law. For simplicity, in both codes, we consider the case of a prescribed driver to excite the IAW and periodic boundary conditions. This model can be regarded as an approach to improve the understanding of the nonlinear saturation of SBS, the coupling of the SBS-driven IAW to the incident and scattered transverse waves being modeled by a given ponderomotive force having the form of a periodic traveling wave. This simplified model makes it possible to study with high spatial and temporal resolutions the interplay between the particle motions and the nonlinear fluid behavior of the driven IAW without the complications of temporal and spatial growths of the transverse waves. The comparison between the results of each type of code enables us to distinguish the respective influence of ion and electron motions on the nonlinear evolution of the driven IAW.

In our paper, we introduce the distinction between the regimes that we name "weak" and "strong" drives, depending on whether the driven IAW amplitude stays below or exceeds the wave-breaking amplitude, respectively. In addition to these two regimes of driving, we carried out simulations in "short" and "long" systems, depending on whether the decay of the driven IAW was quenched or not due to the size of the simulation box. The length of the short system simulation box was chosen to be just one IAW wavelength (λ_m), so that the generation of subharmonics is forbidden. In this case, the IAW nonlinear evolution is determined by the harmonics generation and the kinetic effects only. The length of the long system was chosen to be $8\lambda_m$, so that subharmonics generation could take place. By carrying out additional simulations with longer systems, we checked that we correctly captured the physics in the IAW instabilites.

Our paper is organized as follows: In Sec. II, we describe the hybrid-PIC code and the full-PIC codes. In Sec. III, we present the simulation results in the regimes of weak and strong excitations. In Sec. IV, we attempt to interpret the full-PIC and hybrid-PIC results by comparing them with the results obtained from a simple fluid-type description in which the kinetic effects are modeled by nonlinear frequency shifts. At this stage we are led to present the results of complementary simulations carried out in a short system with the same physical parameters as in the long one, so that the subharmonics generation is quenched. In Sec. V, we investigate the parametric decay instability for an IAW amplitude characteristic of what was observed in the simulations. In Sec. VI, we describe the kinetic effects by inspecting ion and electron phase spaces, and we make some connection with subharmonics generation. Section VII concludes the paper.

II. SIMULATION MODELS

We carried out simulations with two different PIC codes; a full-PIC code, where both particle species were treated kinetically, and a hybrid-PIC code, with kinetic ions and Boltzmann electrons. The equations of motion for the particle species $s = e, i$ described kinetically read

$$d_t x_j = v_j \text{ and } m_s d_t v_j = -q_s \partial_x (\varphi - \varphi_{p,s})|_{x=x_j},$$

where x_j and v_j stand for the particle position and velocity, and q_s and m_s for the charge and the mass, respectively, with $q_e = -e$ for the electrons and $q_i = Ze$ for the ions. The full-PIC code is a prescribed driver version of the code used in the context of SBS in Ref. 4 (and references therein); similarly, the hybrid-PIC code is a prescribed driver version of the 2D code "KOLIPIC,"[26] which is a development of the earlier 1D version documented in Ref. 27. All the simulations presented in this paper correspond to the case of a prescribed driver corresponding to a given potential $\varphi_{p,e}$. The potential $\varphi_{p,i}$ is taken equal to zero. The potential φ is the self-consistent electrostatic potential, satisfying the Poisson equation

$$\epsilon_0 \partial_x^2 \varphi = e(n_e - Z n_i).$$

We use periodic boundary conditions for the particles and fields in all the cases discussed in this paper.

Full-PIC codes require a high time resolution for the electron motion. Hybrid-PIC codes are used in most of the simulations involving IAWs,[6,7,26–29] because they require only the temporal resolution of the IAW time scale. The electron density in hybrid-PIC codes is given by the Boltzmann law

$$n_e(\varphi) = n_{e0} \exp[e(\varphi - \varphi_{p,e})/T_e].$$

Henceforth we consider $\varphi_{p,e}$ as a prescribed driver, the form of which being given by $\varphi_{p,e} = \varphi_d \sin(k_m z - \omega_m t + \text{const})$. The frequency ω_m and wave number k_m satisfy the IAW dispersion relation, $\omega_m = \omega_L(k_m) \equiv c_{s0} k_m [1/(1 + k_m^2 \lambda_{De}^2) + 3T_i/ZT_e]^{1/2}$, with $c_{s0} \equiv (ZT_e/m_i)^{1/2}$ and $\lambda_{De} \equiv (\epsilon_0 T_e/e^2 n_{e0})^{1/2}$ denoting the Debye length.

It should be noted that one of the main differences between each type of codes from the computational point of view, besides the significantly smaller time step in the full-PIC simulations, is the way of solving the Poisson equation. In the hybrid-PIC code, this equation has to be regarded as a nonlinear equation for the potential φ which has to be solved iteratively (following, e.g., Ref. 6). In the full-PIC simulations, the electron density is determined from the electron positions, so that the Poisson equation is simply a linear equation for φ, which has to be integrated for given densities n_e and n_i.

In the hybrid-PIC simulations, the driver is ramped in time up to its maximum value over a few acoustic periods. We checked that our results are very weakly dependent on the rise time of this ramp. In the full-PIC code, the driver was fully switched on from the initial time.

III. IAWS DRIVEN IN A LONG SYSTEM: FULL-PIC VERSUS HYBRID-PIC RESULTS

In this section, we examine two reference cases, representing the regimes of strong and weak excitations of the IAWs. The simulation parameters were chosen in a way to differentiate between the weak and strong ion kinetic effects, in the sense that the IAW interacts with a small number of resonant ions or it gives rise to wave breaking. Let us recall that in the case of a monochromatic IAW characterized by a

potential $\varphi = \varphi_m \sin(k_m z - \omega_m t)$, the ion kinetic effects are able to play some role only if the ion bounce frequency $\omega_{bi} \equiv \omega_m |\phi_m|^{1/2}$ is larger than the linear Landau damping γ_L, where ϕ_m stands for the amplitude of the dimensionless potential $\phi_m = e\varphi_m / T_e$. In the regime $\omega_{bi} > \gamma_L$, the ion velocity distribution function is nonlinearly modified from its initial Maxwellian form. The strong kinetic effects occur in the wave-breaking regime defined by the condition $\delta n_m / n_{e0} > \delta n / n_{e0}|_{WB}$, the wave-breaking limit $\delta n / n_{e0}|_{WB}$ being given by[15]

$$\left. \frac{\delta n}{n_{e0}} \right|_{WB} \equiv \frac{1}{2} \left[\left(\frac{1}{1 + k_m^2 \lambda_{De}^2} + \frac{3T_i}{ZT_e} \right)^{1/2} - \left(\frac{3T_i}{ZT_e} \right)^{1/2} \right]^2 . \tag{1}$$

Here $\delta n_m / n_{e0} \simeq \phi_m$ denotes the relative density-fluctuation amplitude associated with the IAW. We define as weak excitation the regime where the amplitude ϕ_m of the driven IAW stays always below the limit (1). In this regime the perturbative analysis made by Morales and O'Neil[16] holds and the kinetic effects reduce to the nonlinear frequency shift and the nonlinear wave damping. In the strong drive regime, the wave amplitude reaches the wave-breaking limit during the growth phase and no perturbative analysis can be applied.

We selected the following set of normalized parameters for our base line simulations: $k_m^2 \lambda_{De}^2 = 0.1$ and the temperature ratio $T_i / ZT_e = 0.09$, for instance representative of laser-plasma interaction in a plasma characterized by $n_e / n_c \sim 0.1$, $T_e \sim 3$ keV, and $k_m \sim 2k_0$, k_0 denoting the incident laser wave vector and n_c being the electron critical density. The corresponding value of the ion Landau damping is $\gamma_{Li} / \omega_m \sim 0.07$. In the full-PIC simulations, we took $m_i = 1836 m_e$ and the numerical parameters were $\omega_{pe} \Delta t = 0.1$ and $\Delta x = 0.3 \lambda_{De}$ (the ions being pushed every five time steps[30]). In the hybrid-PIC simulations, they were $\omega_{pi} \Delta t = 0.1$ and $\Delta x = 0.3 \lambda_{De}$. Here, $\omega_{pe} \equiv (e^2 n_{e0} / \epsilon_0 m_e)^{1/2}$ and $\omega_{pi} \equiv (Z^2 e^2 n_{i0} / \epsilon_0 m_i)^{1/2}$ denote the electron and ion plasma frequencies, and Δt and Δx are the elementary time and space steps. The number of particles per cell was 200 in the hybrid-PIC simulations and 1000 for each species in the full-PIC simulations.

A. Weak drive regime

We first discuss the typical case of weak drive, corresponding to the driver amplitude $\phi_d \equiv e\varphi_d / T_e = 5 \times 10^{-3}$ and to the long system, the length of the simulation box being eight times the driver wavelength, $\lambda_m \equiv 2\pi / k_m$. The temporal evolution of the normalized fundamental Fourier component $\bar{\phi}_m$ of the potential associated with the driven IAW is illustrated in Fig. 1 from both the full-PIC and the hybrid-PIC simulations.

We denote by t_{max} the time at which the amplitude of the fundamental component $\bar{\phi}_m$ reaches its maximum, denoted as $\overline{\phi_{m,max}}$. It can be seen in Fig. 1 that, past the initial phase of monotonic growth, $\bar{\phi}_m$ decays with irregular oscillations in both types of simulations, to reach a low asymptotic level $\bar{\phi}_m \simeq 1\% - 2\%$, while the driver is still switched on. It should be noted, on the other hand, that t_{max} is shorter, and the
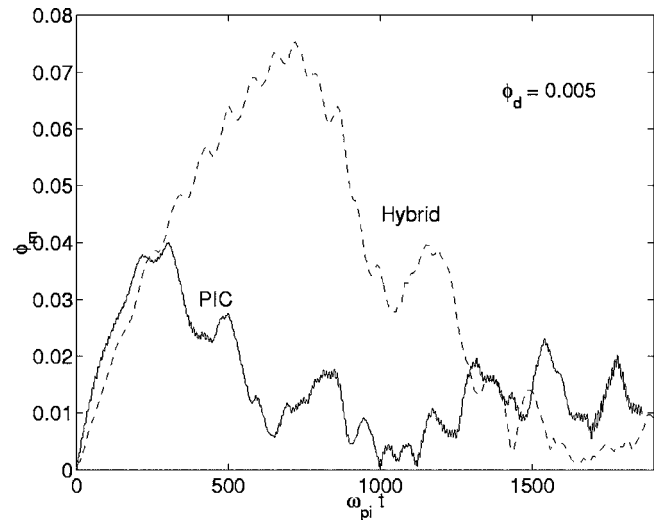

FIG. 1. Amplitude of the fundamental component $\bar{\phi}_m$ vs time, for a driver amplitude $\phi_d = 0.005$ ("weak" drive), $k_m^2 \lambda_{De}^2 = 0.1$, and $T_i / ZT_e = 0.09$. The solid line: full-PIC simulation; the dashed line: hybrid-PIC simulation. System length is $8\lambda_m$.

asymptotic state is reached much earlier, in the case of the full-PIC simulation as compared with the hybrid-PIC simulation.

Figure 2 shows snapshots of the corresponding Fourier spectrum of the electrostatic potential for modes in the interval $0 < k < 4k_m$, in the case of hybrid-PIC simulations. In the initial phase $t < t_{max}$, the driven IAW fundamental component ($k = k_m$) grows to large amplitudes, thus giving rise to a large second- ($k = 2k_m$) and third- ($k = 3k_m$) harmonic amplitudes, as can be seen in panels (a) and (b). It then drops to lower level when the subharmonics generation ($k < k_m$) takes place [panel (c)]. This subharmonics generation develops until the largest amplitudes of the spectrum components correspond to modes with the longest wavelengths, $\lambda \sim (7-8)\lambda_m$ [panel (c)]. Figure 3 shows the counterpart of these results in the case of full-PIC simulations. The comparison shows that the
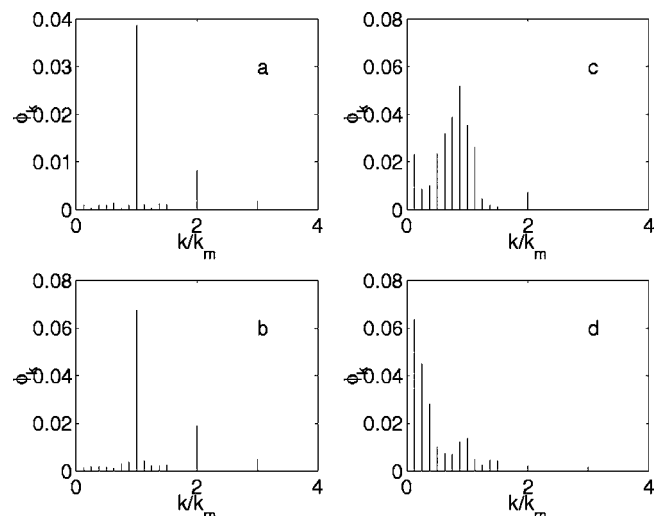

FIG. 2. Snapshots of the IAW Fourier spectrum at four times $\omega_{pi} t = 250$ (a), 600 (b), 1000 (c), 2000 (d). The parameters are the same as in Fig. 1, the hybrid-PIC simulation.
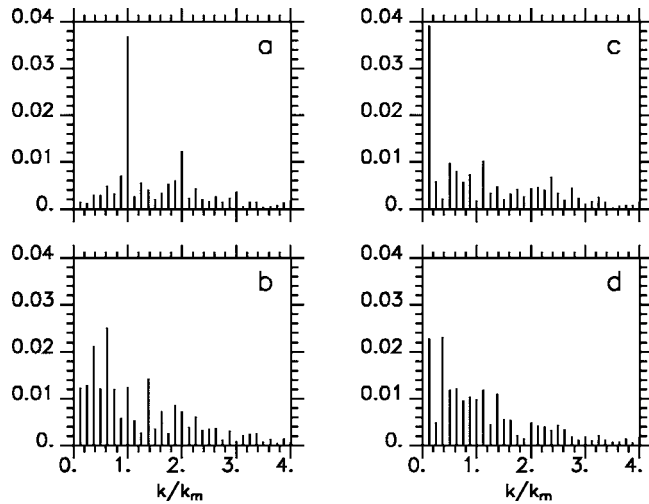
FIG. 3. Snapshots of the IAW Fourier spectrum at four times $\omega_{pi}t=250$ (a), 600 (b), 1000 (c), 2000 (d). The parameters are the same as in Fig. 1, the full-PIC simulation.
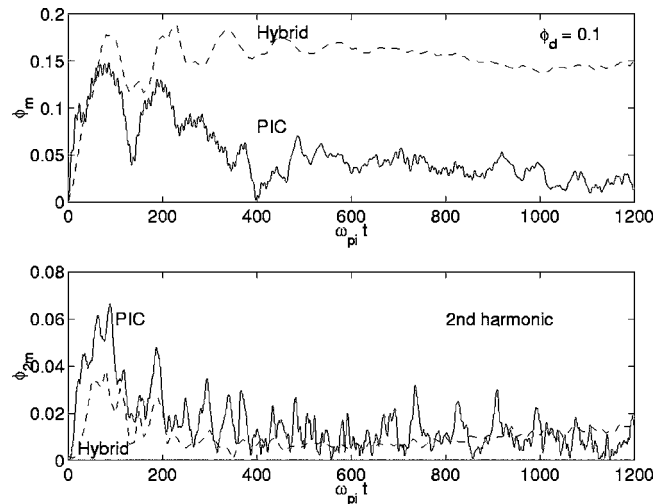

FIG. 4. Amplitude of the fundamental component $\bar{\phi}_m$ vs time, for a driver amplitude $\phi_d=0.1$ (strong drive), with $k_m^2\lambda_{De}^2=0.1$ and $T_i/ZT_e=0.09$. The solid (dashed) line is the result of the full (hybrid)-PIC simulation. System length is $8\lambda_m$.

initial phase during which the spectrum is mainly composed of the fundamental component and of its harmonics is much shorter in the full-PIC case; in particular, panel (b) exhibits already subharmonics generation for k around k_m, a feature that could be seen only at later times [Fig. 2(c)] in the hybrid-PIC case. The comparison between panels (c) and (d) in Fig. 3 indicates that the spectral density does not vary much as a function of k in the interval $k_m/2 < k_m < 3k_m$, by contrast with the hybrid-PIC results [Fig. 2(d)]. Finally, it should be pointed out that for both types of simulations, the driven mode amplitude ($k=k_m$) does not exceed the neighboring mode amplitudes, in the long-time behavior, although the system remains driven.

B. Strong drive regime

In the case of strong IAW drive, $\phi_d=0.1$, the time evolution of the fundamental Fourier component $\bar{\phi}_m$ shows a striking difference between the full-PIC and the hybrid-PIC simulations, as can be seen in Fig. 4. In this case, the IAW amplitude exceeds the wave-breaking limit (1), $\bar{\phi}_m|_{WB} = \delta n/n_{e0}|_{WB}=0.14$ for the present parameters. While in the full-PIC description the driven IAW overshoots the wave-breaking limit and quickly drops to much smaller values with significant subharmonics generation; in the hybrid-PIC simulation the mode amplitude reaches the wave-breaking limit and then stabilizes slightly above this level. In Fig. 4 we also plot the second-harmonic amplitude $\bar{\phi}_{2m}$ as a function of time. It is interesting to remark that at early times there is a significant difference in the $\bar{\phi}_{2m}$ amplitudes between the two types of simulations, while the $\bar{\phi}_m$ amplitudes are about the same. This result will be interpreted in Sec. IV as due to the nonlinear frequency shift due to electrons. By contrast, in the long-time limit, the $\bar{\phi}_{2m}$ amplitudes are comparable in the two types of simulations, whereas the $\bar{\phi}_m$ amplitudes are significantly different. We interpret the level of the $\bar{\phi}_{2m}$ amplitude in the PIC simulation as due to the fact that it is enslaved to $\bar{\phi}_m$, so both are small; concerning the hybrid-PIC

simulation we will interpret in Sec. IV the smallness of $\bar{\phi}_{2m}$ as due to the nonlinear frequency shift due to strong ion kinetic effects.

In Fig. 5 we show snapshots of the corresponding Fourier spectrum of the electrostatic potential in the case of hybrid-PIC simulations. At all times one can see a relatively large value for the fundamental amplitude $\bar{\phi}_m$, some harmonics generation at early times, but only a negligibly small level of harmonics and subharmonics for long times. The driven IAW grows until it reaches a stable equilibrium. By looking at the ion phase space, this steady-state behavior is seen to take place together with trapping of a large number of ions, which is a reminiscence of a stable Berstein-Greene-Kruskal (BGK) mode. As will be seen in Sec. V, such a
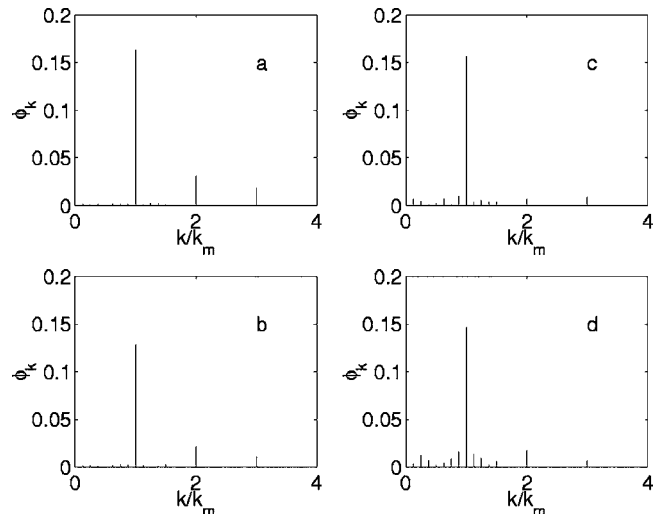

FIG. 5. Snapshots of the Fourier spectrum at four times $\omega_{pi}t=70$ (a), 150 (b), 400 (c), 1500 (d). The parameters are the same as in Fig. 4, the hybrid-PIC simulation.
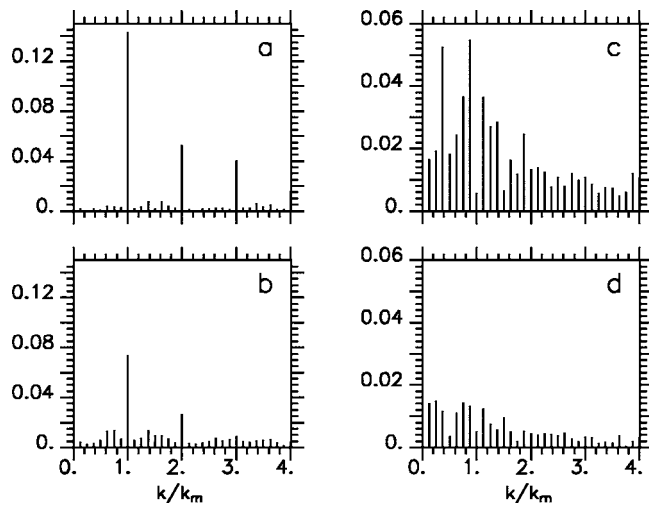
FIG. 6. Snapshots of the Fourier spectrum at four times $\omega_{pi}t=70$ (a), 150 (b), 400 (c), 1500 (d). The parameters are the same as in Fig. 4, the full-PIC simulation.
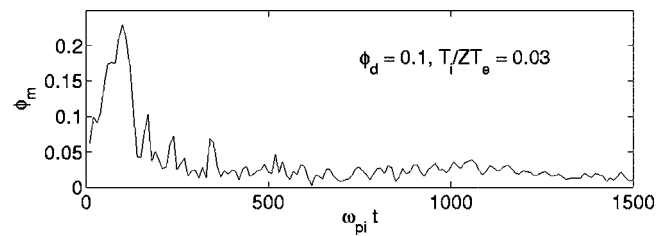

FIG. 7. Amplitude of the fundamental component $\bar{\phi}_m$ vs time, for a driver of amplitude $\phi_d=0.1$, $k_m^2\lambda_{De}^2=0.1$, and $T_i/ZT_e=0.03$.

stabilization for high amplitude is interpreted consistently with the stability analysis of the IAW decay in the presence of ion kinetic effects.

By contrast, no similar stabilization of the fundamental component $\bar{\phi}_m$ is observed in the full-PIC simulation. Even if the IAW amplitude exceeds the wave-breaking limit in the phase of initial growth, it decreases rapidly to much smaller values at longer times. In Fig. 6 we plot snapshots of the Fourier spectrum of the electrostatic potential corresponding to the full-PIC simulations. It can be seen that the temporal decay of the fundamental component, together with the temporal growth of its subharmonics, is similar to what was observed in the case of weak excitation (Fig. 3), but they occur on a shorter time scale. The final spectrum is roughly a uniform function of k, with the level of $|\phi_k|\lesssim 0.02$. By looking at the ion phase space, it can be seen that the subharmonics generation takes place together with a smooth modification of the distribution function corresponding to a diffusion in the velocity space. These features will be discussed in more detail in Sec. VI.

We have carried out other simulations with higher driver amplitudes than for our base line strong drive simulation, and we found that the scenario remains essentially the same. The differences between the full-PIC and the hybrid-PIC simulations appear to be more pronounced for stronger drive. In the case of hybrid-PIC simulations, the fundamental mode amplitude $\bar{\phi}_m$ can significantly exceed the wave-breaking limit, and then it stays at a level as high as $|\phi_m|=\delta n_m/n_{e0}$ ~ 0.2. In this regime, a large population of ions is trapped. As in the case of the base line strong drive simulation, there is neither significant harmonics growth nor subharmonics generation, with a few exceptions when the subharmonics appear for a transient stage. In the full-PIC simulations, the amplitude of the fundamental component $\bar{\phi}_m$, after the initial secular growth, saturates at a level almost independent of the driver. For example, in the case of $\phi_d=0.25$, the fundamental mode slightly overshoots the wave-breaking limit, $\bar{\phi}_m$ ~ 0.15, and then it drops to much smaller values over a few

ion sound wave periods. This process is accompanied by a subharmonics generation and a strong diffusion in the ion velocity space.

C. Lower ion temperatures

We carried out additional simulations with T_i/ZT_e $=0.03$ in order to investigate the role of the ion temperature. This lower-temperature ratio leads to two main differences from the previously discussed cases: (i) the ion Landau damping is much smaller, so that the IAW damping is due to the electrons in the full-PIC simulations, with γ_L/ω_m $\simeq 0.012$; (ii) the ion wave-breaking limit, $|\delta n/n_{e0}|_{\text{WB}}\sim 0.22$, is significantly larger. Nevertheless, the scenarios, for each type of simulations (full PIC or hybrid PIC), and for each kind of drive (weak or strong), remain essentially similar to those discussed before for our base line simulations. Simply, the IAW grows to larger amplitudes, so that the fluid-type effects, such as harmonics generation, are more pronounced in the initial phase of secular growth, before the wave breaking occurs.

For the simulations carried out in the weak excitation regime, the amplitude of the driven wave reaches amplitudes of the order of $\bar{\phi}_m=0.04-0.05$, then decreases to the level $\bar{\phi}_m=0.02-0.03$, for both hybrid-PIC and full-PIC simulations. The main difference is that the IAW amplitude decreases on a considerably shorter time scale in the full-PIC case, demonstrating again the importance of the electron kinetic effects. In the hybrid-PIC case, the amplitude of fundamental component stays longer time at high level providing more efficient harmonics and subharmonics generations.

In the hybrid-PIC simulation carried out in the strong excitation regime, we observe the initial phase of secular growth of the driven IAW, followed by small oscillations at the level of $\phi_m\approx 0.1-0.2$. In the full-PIC simulation, the amplitude of the driven IAW, displayed in Fig. 7, grows secularly in the first phase when the harmonics generation takes place. At the time of wave breaking, subharmonics generation occurs, initially characterized by a spectrum localized around the half harmonic $k=k_m/2$. Then the spectrum extends to the whole range $k\lesssim k_m$, and the driven IAW amplitude drops to very small values. These results will be discussed in more detail in Sec. VI in association with the analysis of the ion phase space. It will be seen in Fig. 16 that the spatial period doubling associated with the half-harmonics generation appears very clearly in the ion phase space.
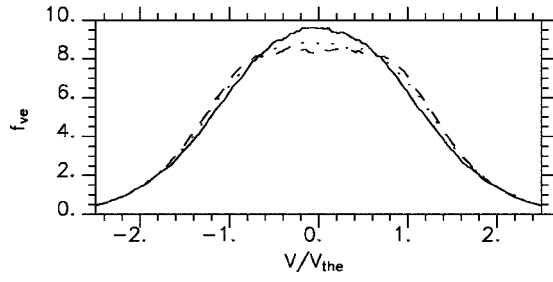
FIG. 8. Electron distribution function showing subsequent flattening at times $\omega_{pi}t = 0$, 180, and 1500. The parameters are the same as in Fig. 4, the full-PIC simulation.

D. Electron distribution function in full-PIC simulations

The main feature concerning the electron kinetic effects is the flattening of the electron distribution function in the domain of small velocities $v \lesssim v_{\text{the}}$, where $v_{\text{the}} = \sqrt{T_e/m_e}$ is the electron thermal velocity (see Fig. 8). The higher the driver amplitude, the more pronounced is the flattening. In order to quantify this result, we approximated the electron distribution by the hyper-Gaussian function,

$$f_e^{\text{HG}}(v) = \frac{\alpha}{\sigma v_{\text{the}}} 2^{-1-1/\alpha} \Gamma^{-1}\left(\frac{1}{\alpha}\right) \exp\left[-\frac{1}{2}\left(\frac{|v|}{\sigma v_{\text{the}}}\right)^\alpha\right], \quad (2)$$

characterized by two parameters; the exponent α and the width σ in velocity space. The Maxwellian distribution function corresponds to $\alpha = 2$ and $\sigma = 1$. In the weak drive regime, α and σ remain very close to the Maxwellian limit for the entire duration of the simulation, with $\alpha \simeq 2.02 - 2.04$ and $\sigma \simeq 1.01 - 1.02$. In the strong drive regime, the parameters α and σ initially increase rapidly to $\alpha \simeq 2.6$ and $\sigma \simeq 1.2$ within the period of time $\omega_{pi}t < 400$. Then they grow more slowly until they reach $\alpha \simeq 2.85$ and $\sigma \simeq 1.27$ at the time $\omega_{pi}t \sim 1500$.

This latter value for σ corresponds to a very significant modification of the IAW spectrum and damping. Let us define by $\omega_{\text{kin},e}(k)$ the solution to the dispersion relation in which the electron susceptibility is computed in terms of the electron distribution function (2) with the parameters α and σ measured in the simulations. Then for the frequency shift $\delta\omega_{\text{kin},e}(k) \equiv \omega_{\text{kin},e}(k) - \omega_L(k)$ one finds at lowest order

$$\delta\omega_{\text{kin},e}/kc_{s0} = \sigma 2^{1/\alpha} \alpha^{-1/2} [\Gamma(1/\alpha)/\Gamma(1-1/\alpha)]^{1/2} - 1. \quad (3)$$

In Table I, we reported the values of the two parameters α and σ obtained by a best fit of the electron distribution func-

tion $f_e(v)$ measured at the final time of our simulations. We have also reported the values of the corresponding frequency shift (3). It can be seen that the interaction of the IAW with electrons leads to an increases of the mode frequency and of its phase velocity. The positive sign of $\delta\omega_{\text{kin},e}$ can be easily understood as follows: the flattening of the electron distribution function can be viewed as an increase of the Debye length, from which follows expression (3) for $\delta\omega_{\text{kin},e}$. The following sections are devoted to a detailed discussion of the modeling of the kinetic effects.

IV. FLUID-TYPE MODELING OF THE KINETIC EFFECTS

The modifications of the electron and ion distribution functions caused by the existence of a large amplitude IAW lead to changes in the dispersion relation, which becomes a function of time. We denote by $\omega_{\text{kin}}(k)$ and by $-\gamma_{\text{kin}}(k)$ the real and imaginary parts of the instantaneous solution to the modified dispersion relation. Consistently with the definition of the nonlinear electron frequency shift (3) introduced in the previous section, we define more generally the nonlinear frequency shift $\delta\omega_{\text{kin}}$ as $\delta\omega_{\text{kin}}(k) \equiv \omega_{\text{kin}}(k) - \omega_L(k)$.

In Ref. 25, we examined the possibility of modeling the full-PIC and hybrid-PIC simulation results by means of a fluid-type description consisting in two coupled equations for $\bar{\phi}_m$ and $\bar{\phi}_{2m}$. In the initial phase of monotonic growth of the fundamental component $\bar{\phi}_m$, the kinetic effects were modeled by the nonlinear frequency shift $\delta\omega_{\text{kin}} = \omega_m \eta |\bar{\phi}_m|^{1/2}$, with $\eta = \eta_i + \eta_e$ accounting for the contributions of ions and electrons. The hybrid-PIC simulations correspond to $\eta_e = 0$. The damping of the fundamental mode and its harmonic were modeled by the simple time dependence $\gamma_m(t) \equiv \gamma_L(k_m)/(1 + t/\tau_{\text{bi}})$ and $\gamma_{2m}(t) \equiv \gamma_L(2k_m)/(1 + t/\tau_{\text{bi}})$, where $\tau_{\text{bi}} = (2\pi/\omega_m)|2\bar{\phi}_m|^{-1/2}$ is the ion bounce time.

In the case of a monochromatic wave and the initial condition (IC) problem, the parameter η_i was predicted to be[16]

$$\eta_i^{\text{IC}} = -2.2\sqrt{2}c_{s0}(\omega_m/k_m)^2 \partial_v^2 f_{i0}. \quad (4)$$

This expression leads to a negative value for η_i^{IC} in the limit $v_{\text{ph}} = \omega_m/k_m > v_{\text{thi}}$, which is the case. Here, f_{i0} denotes the initial ion distribution function and $v_{\text{thi}} = \sqrt{T_i/m_i}$ is the initial thermal velocity. A similar expression was then derived in the case of a driven system with a slightly different coefficient.[17] A positive frequency shift, $\eta_e^{\text{IC}} = 0.22\sqrt{2}(1 + k_m^2\lambda_{\text{De}}^2)^{-3/2}$, was predicted in Ref. 31 for what concerns the

TABLE I. Coefficients α and σ defining the electron distribution function (2) measured in the simulations at their final time. We have also reported the corresponding relative nonlinear frequency shift $\delta\omega_{\text{kin},e}/kc_{s0}$ of the IAW frequency. The last two columns indicate the maximum value $\bar{\phi}_{m,\text{max}}$ of the driven IAW amplitude reached during the simulation and the amplitude $\bar{\phi}_{m,\text{end}}$ at the final time.

T_i/ZT_e	ϕ_d	α	σ	$\delta\omega_{\text{kin},e}/kc_{s0}$	$\bar{\phi}_{m,\text{max}}$	$\bar{\phi}_{m,\text{end}}$
0.09	0.005	2.041	1.018	0.018	0.04	0.01
0.09	0.1	2.850	1.268	0.24	0.18	0.02
0.03	0.005	2.059	1.027	0.028	0.04	0.02
0.03	0.1	3.55	1.445	0.37	0.24	0.01

electrons. However, this result was not confirmed later.[17] Independently of the various expressions for the electron nonlinear frequency shift, we believe that the flattening of the electron distribution function for $v < v_{\text{the}}$, as observed in our simulations, gives rise to a positive frequency shift. This has been discussed in Ref. 9 and it is in agreement with the values of $\delta\omega_{\text{kin},e}(k)$ reported in Table I.

In this section, we investigate whether it is possible to determine a value of the parameter η such that our simulation results, *during* the initial phase of monotonic growth, could be correctly described by coupled-mode equations in which the kinetic effects are simply modeled by the nonlinear frequency shift $\delta\omega_{\text{kin}}(k) = \omega_L(k)\eta|\bar{\phi}_m|^{1/2}$, and by the time-dependent damping $\gamma_k(t) = \gamma_L(k)/(1 + t/\tau_{\text{bi}})$. In the next section, we will consider the more difficult question concerning whether this simple coupled-mode description can be used to determine the time at which the subharmonics generation takes place.

The coupled-mode equations describing the evolution of amplitudes of the fundamental component $\bar{\phi}_m$ and its second harmonic $\bar{\phi}_{2m}$ can be easily derived from the Korteweg–de Vries equation for an ion acoustic wave. They can be written as

$$[\partial_t + \gamma_m(t) + i\delta\omega_{\text{kin}}]\phi_m = -i\omega_m(\bar{\phi}_{2m}\bar{\phi}_m^* + \phi_d/4), \tag{5}$$

$$[\partial_t + \gamma_{2m}(t) + 2i\delta\omega_{\text{kin}} + i\delta\omega_{\text{disp}}]\bar{\phi}_{2m} = -i\omega_m\bar{\phi}_m^2, \tag{6}$$

where $\delta\omega_{\text{disp}} = \omega_L(2k_m) - 2\omega_L(k_m) = 3k_m^2\lambda_{\text{De}}^2\omega_m$ denotes the frequency mismatch caused by the IAW dispersion and $\delta\omega_{\text{kin}} = \omega_m\eta|\bar{\phi}_m|^{1/2}$ denotes the nonlinear frequency shift corresponding to the fundamental component. Equation (6) may be simplified, because the second-harmonic amplitude appears, in the numerical simulations, to be strongly enslaved to the fundamental component. This allows us to neglect the time derivative and the damping in Eq. (6) and to approximate the second harmonic by $\bar{\phi}_{2m} \simeq \bar{\phi}_m^2/\Delta_2$ with $\Delta_2 \simeq 3k_m^2\lambda_{\text{De}}^2 - 2\eta|\bar{\phi}_m|^{1/2}$. One then obtains a single nonlinear differential equation for the fundamental component,

$$([\partial_t + \gamma_m(t) + i\delta\omega_{\text{nl}}]\bar{\phi}_m = -\frac{i}{4}\omega_m\phi_d, \tag{7}$$

where $\delta\omega_{\text{nl}}(\bar{\phi}_m) \equiv \omega_m(\eta|\bar{\phi}_m|^{1/2} + |\bar{\phi}_m|^2/\Delta_2)$ is the total nonlinear frequency shift. This equation can be further simplified by noticing that the damping and the second-harmonic contribution in the nonlinear term play a role only at the moment when the amplitude $\bar{\phi}_m$ is close to its asymptotic value, that we denote as $\bar{\phi}_{m,\text{sat}}$. For this reason, we replace $\bar{\phi}_m$ by $\bar{\phi}_{m,\text{sat}}$ in the expressions of τ_{bi}, appearing in the definition of $\gamma_m(t)$, and in the expression of Δ_2, which becomes then $\Delta_{2,\text{sat}} \equiv 3k_m^2\lambda_{\text{De}}^2 - 2\eta|\bar{\phi}_{m,\text{sat}}|^{1/2}$. The value of $\bar{\phi}_{m,\text{sat}}$ is known from the numerical simulations.

Equation (7) contains only one free parameter η. This single parameter can therefore be determined accurately by finding the solution to Eq. (7) which represents the best fit of the amplitude $\bar{\phi}_m(t)$ provided by the numerical simulations. Moreover by comparing the solution to Eq. (7) with the simulations carried out in the short simulation box, where the
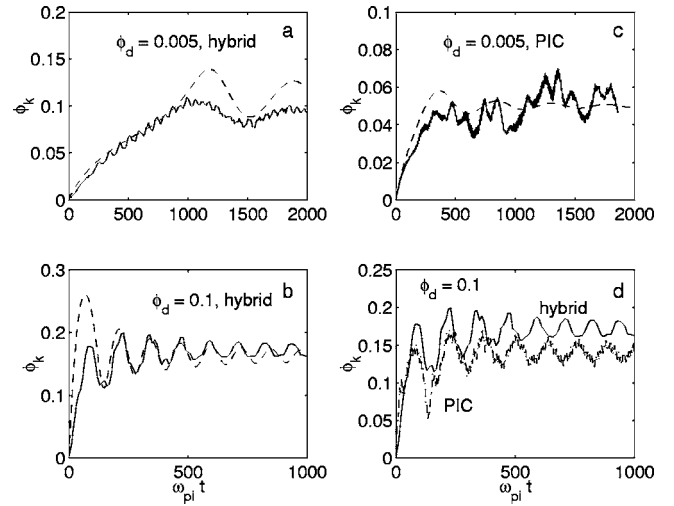

FIG. 9. Amplitude of the fundamental component $\bar{\phi}_m$ vs time, for (a) [top left] $\phi_d = 0.005$, the hybrid-PIC simulation; (b) [bottom left] $\phi_d = 0.1$, the hybrid-PIC simulation; (c) [top right] $\phi_d = 0.005$, the full-PIC simulation. The result of the simulations is compared with the solution of the model equation (7) (solid line). (d) [Bottom right] Comparison between the hybrid-PIC and full-PIC simulations for $\phi_d = 0.1$. The other parameters are $k_m^2\lambda_{\text{De}}^2 = 0.1$ and $T_i/ZT_e = 0.09$. All simulations are done in a short box of the length of $1\lambda_m$.

subharmonics generation is quenched, we may extend the study of the kinetic effects on a significant longer time. By proceeding along this way we were able to improve the accuracy of η. We numerically integrated Eq. (7) for a given value of η, taking $\bar{\phi}_{m,\text{sat}}$ equal to the saturation amplitude of $\bar{\phi}_m$ observed in the simulations carried out in the short box. Then, we varied η in order to optimize the fit of $\bar{\phi}_m(t)$. The results of these best fits are displayed in the four panels of Fig. 9, describing the hybrid-PIC and the full-PIC simulations, for the weak and strong drive regimes. They are discussed in detail in Sec. IV A. At this point, it is worth to note that the differences which can be clearly observed in panels (a) and (b) between the hybrid-PIC and full-PIC simulation results in the weak drive regime can only be attributed to the electron kinetic effects.

Finally, we checked *a posteriori* the consistency of our procedure as follows: having determined the value of η from the best fit of $\bar{\phi}_m(t)$, we computed the corresponding prediction for the second-harmonic amplitude $\bar{\phi}_{2m}(t)$ at the time of saturation, denoted as $\bar{\phi}_{2m,\text{sat}}(t)$. This quantity is predicted to be given by $\bar{\phi}_{2m,\text{sat}} \simeq \bar{\phi}_{m,\text{sat}}^2/\Delta_{2,\text{sat}}$ within the coupled-mode description. We therefore consider that the coupled-mode equations [(5) and (6)] and valid descriptions of the simulation results, whenever (i) the best fit of $\bar{\phi}_m(t)$ is good and (ii) the prediction $\bar{\phi}_{m,\text{sat}}^2/\Delta_{2,\text{sat}}$ for the asymptotic value of the second-harmonic amplitude $\bar{\phi}_{2m,\text{sat}}$ is close to the numerical simulations.

A. Ion frequency shift from the hybrid-PIC simulations

In the weak excitation regime and in the case of hybrid-PIC simulations, the results displayed in Fig. 9(a) indicate

$|\bar{\phi}_{m,\text{sat}}| \simeq 0.09$. The best-fit procedure explained in the introduction of this section leads to $\eta_i = -0.13$. This value was obtained by taking the ion bounce time $\omega_{pi}\tau_{\text{bi}} = 100$ and $\gamma_L/\omega_m = 0.05$, consistent with the numerical simulation values. Inspection of Fig. 9(a) shows that the best fit is good: the results of the hybrid-PIC simulations agree very well with the solution to Eq. (7). The corresponding value for the parameter Δ_2 is $\Delta_{2,\text{sat}} = 0.35$, leading to the result $|\bar{\phi}_{2m,\text{sat}}| = 0.025$, which is found to be in good agreement with the numerical simulation results. We may therefore conclude to the validity of the fluid-type description in this case with $\eta_i = -0.13$. It is interesting to compare this result with the theoretical prediction (4), leading to a higher value of $\eta_i \sim -0.68$. We interpret the difference with our best fit by the fact that Morales and O'Neil's theoretical prediction was derived in the context of an initial value problem and not in the case considered here of an externally driven system.

We proceeded in the same way for the strong excitation regime and in the case of hybrid-PIC simulations. The simulation results displayed in Fig. 9(b) indicate $|\bar{\phi}_{m,\text{sat}}| \simeq 0.15$, which is close to the wave-breaking limit. The best-fit procedure leads to $\eta_i = -0.5$, corresponding to the nonlinear frequency shift $\delta\omega_{\text{kin},i} \simeq -0.2$. This value was obtained by taking the ion bounce time $\omega_{pi}\tau_{\text{bi}} = 50$ and $\gamma_L/\omega_m = 0.05$, consistent with the numerical simulation values. Inspection of Fig. 9(b) shows that the best fit is indeed very good. The value of the parameter Δ_2 is $\Delta_{2,\text{sat}} = 0.7$, leading to the prediction $|\bar{\phi}_{2m,\text{sat}}| = 0.03$, which is found to be in reasonably good agreement with the numerical simulation results. Thus, similar to the weak excitation regime, we may conclude to the validity of our fluid-type description in this strong excitation case, the value of η_i being now -0.5. It could seem surprising that two valid best fits do not lead to the same value for the parameter η_i, when the physical parameters (besides the driver amplitude) are identical in each of the simulations. We interpret this result by the fact that in the strong drive regime, ion wave breaking occurs very early in the simulations, so that the ion distribution function is deeply modified in the velocity range close to the IAW phase velocity.

Thus, our results seem to show that the fluid-type equations in which the kinetic effects are modeled by a nonlinear frequency shift proportional to the square root of the wave amplitude, remain a valid description in the strong drive regime, even though there is not yet any theory available to predict the value of the parameter η_i, because (i) the excited IAW is externally driven and (ii) there is an effective heating caused by the strong kinetic effects. Further work is obviously needed, in particular, concerning the IAW damping in the case of ion tail formation. The ion kinetic effects and their interplay with the IAW damping are discussed in more details in Sec. VI.

B. Partial validity of the fluid-type description for the full-PIC simulations

In the weak excitation regime and in the case of full-PIC simulations, the results displayed in Fig. 9(c) indicate $|\bar{\phi}_{m,\text{sat}}| \simeq 0.05$. The best-fit procedure leads to $\eta \simeq 0$. This

value was obtained by taking the ion bounce time $\omega_{pi}\tau_{\text{bi}} = 100$ and $\gamma_L/\omega_m = 0.05$. Inspection of Fig. 9(c) shows that the best fit seems to be very good. However, it is inconsistent with the second-harmonic amplitude. The value of the parameter Δ_2 is $\Delta_{2,\text{sat}} = 0.3$, leading to the prediction $|\bar{\phi}_{2m,\text{sat}}| = 0.0008$, which is lower by a factor of 2 than the simulation result $|\bar{\phi}_{2m,\text{sat}}| = 0.0018$ (this value being obtained by averaging over several temporal oscillations).

In order to gain some insight concerning the origin of the failure of the fluid-type description, we cross-checked the value of η determined by the best-fit procedure, with the expression $\eta = \eta_i + \eta_e$ in which two parts were evaluated as follows: concerning the ion contribution, we used the result $\eta_i = -0.13$ found in Sec. IV A for the weak drive regime; concerning the electron contribution, η_e was obtained from the direct computation of the nonlinear frequency shift $\delta\omega_{\text{kin},e}$ following the procedure outlined in Sec. III [Eq. (3)]. The value $\delta\omega_{\text{kin},e} = 0.018\omega_m$ reported in Table I leads to $\eta_e = 0.09$. Consequently, the total frequency shift $\delta\omega_{\text{kin}} = \omega_m \eta_i |\bar{\phi}_{m,\text{sat}}|^{1/2} + \delta\omega_{\text{kin},e} \simeq -0.01\omega_m$ agrees very well with the value $\delta\omega_{\text{kin}} \simeq 0$ obtained from the best-fit procedure. Therefore, we must conclude that the fluid-type description in which the kinetic effects are modeled by a nonlinear frequency shift can describe only qualitatively the initial phase dynamics in the full-PIC simulations, even though there is a good agreement between the best-fit procedure to determine η and the direct computation of the frequency shift from the distribution function.

In order to evaluate the contribution of the subharmonics in the temporal evolution of the IAW amplitude, other simulations have been performed with the short simulation box of length λ_m. The results of the hybrid-PIC and full-PIC simulations in the strong drive regime are presented in Fig. 9(d). For both types of simulations, the system evolves in such a way that asymptotically it reaches a very well-defined equilibrium, with a large fundamental component amplitude. Inspection of the ion phase space shows the existence of a large population of trapped ions. We could not find any satisfactory best fit to the full-PIC simulations in this strong drive regime.

V. ION ACOUSTIC DECAY IN THE PRESENCE OF KINETIC EFFECTS

In this section we investigate whether the fluid-type description presented in Sec. IV makes it possible to determine the characteristic time scale t_{max} on which the subharmonics generation takes place. This fluid-type description contains two effects: (i) the quadratic fluid nonlinearity, such as in the Korteweg–de Vries equation, and (ii) the nonlinear frequency shift modeling the kinetic effects. We therefore consider our base line simulations carried out in the long simulation box and investigate whether the time t_{max} can be interpreted as the characteristic time for the development of this parametric decay instability.

The dispersion relation for the parametric IAW decay has been derived in Ref. 32. It considers the stability of a stationary weakly nonlinear IAW ($\bar{\phi}_m$, $\bar{\phi}_{2m}$) in the presence of a frequency mismatch $\delta\omega_{\text{mis}}$. This dispersion relation de-
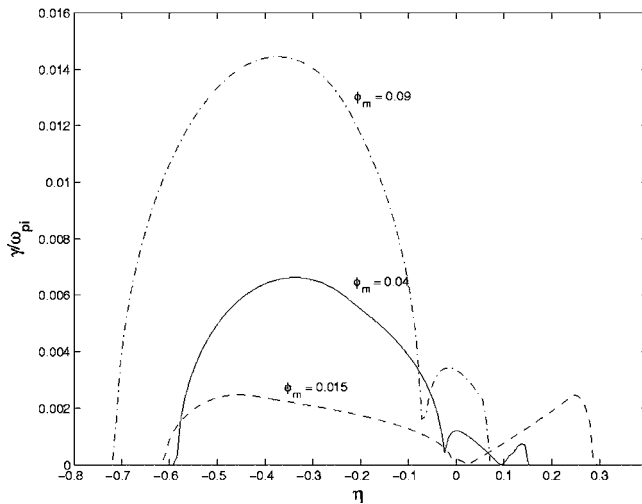
FIG. 10. Normalized growth rate γ/ω_{pi} vs the detuning parameter η for $k_m^2\lambda_{De}^2=0.1$ and for three values of the the IAW amplitudes $\bar{\phi}_m=0.015$, 0.04, and 0.09.

scribes two types of IAW instabilities associated with the fluid nonlinearity: the modulational instability in the case of the positive nonlinear frequency shift, $\eta>0$, and the decay instability (the so-called two-ion decay) in the opposite case, $\eta<0$. We generalize this result by considering $\delta\omega_{mis}=-\delta\omega_{kin}=-\omega_m\eta|\bar{\phi}_m|^{1/2}$. The corresponding dispersion relation has been solved numerically. The maximum growth rate as a function of the parameter η is shown in Fig. 10 for $k_m^2\lambda_{De}^2=0.1$ and for three values of the IAW amplitude $\bar{\phi}_m=0.015$, 0.04, and 0.09. The domain of the amplitudes is limited by the condition of validity of the stability analysis $\bar{\phi}_m\lesssim k_m^2\lambda_{De}^2$. It can be seen that for the largest $\bar{\phi}_m$ considered in the figure, the instability growth rate is non-negligible only in the domain of negative detuning (corresponding to the two-ion decay) and provided that η satisfies $\eta>\eta_{co}$, with the cutoff value $\eta_{co}<0$. By contrast, for small $\bar{\phi}_m$ the growth rates are comparable for positive (modulational instability) and negative (two-ion decay) detunings.

Let us first consider the weak drive regime. In the full-PIC simulations, the fundamental component amplitude $\bar{\phi}_m$ reaches the maximum amplitude $\overline{\phi_{m,max}}=0.04$. Taking then $\bar{\phi}_m=0.04$ and $\eta\simeq0$ as found in the previous section, the solution to the dispersion relation leads to the growth rate γ which is smaller than $10^{-3}\omega_{pi}$. The short saturation time $t_{max}\simeq300\omega_{pi}^{-1}$ observed in the full-PIC simulations cannot be explained by such an instability. By contrast, in the hybrid-PIC simulations the fundamental component amplitude $\bar{\phi}_m$ is of the order of the maximum amplitude $\overline{\phi_{m,max}}=0.07$. Assuming then $\eta=-0.13$, as found in the previous section, one finds the growth rate $\gamma=8\times10^{-3}\omega_{pi}$. This value is in good agreement with the saturation time $t_{max}\simeq700\omega_{pi}^{-1}$ observed in the hybrid-PIC simulations and corresponding to a gain factor of a few units. These results confirm our previous findings concerning the weak drive regime: (i) the ion kinetic effects appear to be properly modeled by the nonlinear frequency shift; (ii) accepting this fact, one must conclude that the electron kinetic effects cannot be reduced to a simple

nonlinear frequency shift and involve another process which makes the IAW more unstable than in the case where they are ignored.

In the strong drive regime, the driven IAW asymptotic behavior differs significantly between the two types of simulations, as can be seen in Fig. 4(a). The full-PIC simulations lead to the same scenario as in the weak drive regime: after an initial secular growth, at the time $t_{max}\simeq80\omega_{pi}^{-1}$ $\bar{\phi}_m$ reaches the large value $\overline{\phi_{m,max}}=0.15$. Past this time t_{max} the fundamental component amplitude decreases with irregular oscillations to the low level $\bar{\phi}_m\simeq0.02$. By contrast, in the hybrid-PIC simulations, $\bar{\phi}_m$, past a quasimonotonic growth, reaches a quasisteady state, with $\bar{\phi}_m\sim0.15$. This value of $\bar{\phi}_m$ being larger than $k_m^2\lambda_{De}^2$, this case is in principle outside the domain of validity of the stability analysis. However, even if we do not have a fully quantitative explanation of the dramatic difference between the full-PIC and hybrid-PIC results, we are able to interpret qualitatively this difference from the general tendency of the dependence of the instability growth rate as a function of the parameter η. Indeed, as mentioned above, Fig. 10 shows that the driven IAW is predicted to be stable whenever η is negative, with $\eta<\eta_{co}$. In the case of hybrid-PIC simulations, we estimated $\eta\sim-0.5$ in the strong drive regime. In the case of full-PIC simulations, we did not find a satisfactory estimate of η. However, we may expect that the electron kinetic effects give rise to a positive nonlinear frequency shift, so that, as compared to the hybrid case, the absolute value of η is reduced, or even η is positive. We can thus interpret the difference between the hybrid-PIC and the full-PIC simulations by associating this difference with the value of the parameter η. In the hybrid-PIC simulation η is negative and, we hypothesize, lower than the treshold value η_{co}, so that the IAW is stable; in the full-PIC simulation η is larger, which makes the IAW unstable.

VI. INTERPLAY BETWEEN PARAMETRIC DECAY AND KINETIC EFFECTS

We have seen in the previous sections that the kinetic effects may favor the parametric instability of a quasimonochromatic IAW. In this section, we will see that, conversely, the decay of the fundamental component of the IAW driven wave into subharmonics induces an additional modification of the distribution functions, especially in the strong drive case. We begin with examining the electron and ion phase spaces before and after subharmonics generation. Then, we estimate the particle heating and show that the absorbed energy goes essentially into the ions. Therefore we can attribute the IAW damping in the strong drive case to the ion kinetic effects. From these results emerges the following scenario: (i) the electron kinetic effects favor the subharmonics decay because the associated frequency shift balances partly the ion contribution (in particular, in the regimes where the latter are so strong that they would lead to a stable BGK-like quasimonochromatic wave); (ii) the subharmonics decay in turn favors diffusion in ion phase space, leading to additional effective IAW damping; (iii) the additional damping provokes an even faster decrease of the driven IAW amplitude. The validity of these conclusions is confirmed at the end of
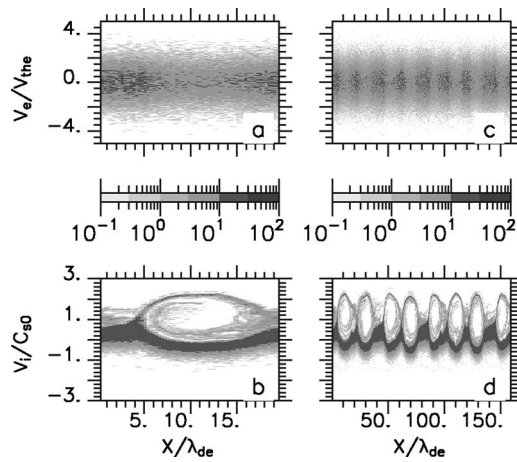
FIG. 11. Electron [(a) and (c)] and ion [(b) and (d)] phase spaces at $\omega_{pi}t$ =200, for the same parameters as in Fig. 4 ("strong" drive); [(a) and (b)] short box of $1\lambda_m$ and [(c) and (d)] long box of $8\lambda_m$.

FIG. 13. Electron and ion phase spaces at $\omega_{pi}t$=1480, for the same parameters as in Fig. 4 (strong drive); [(a) and (b)] box length is $1\lambda_m$ ("short" box) and [(c) and (d)] box length is $8\lambda_m$.

this section by examining their sensitivity on the ion-to-electron temperature ratio and the length of the simulation box.

A. Kinetic effects caused by the subharmonics generation

The subharmonics generation has little effect on the ion phase space in the weak drive case. The ions accommodate gently to the generation of the subharmonics modes, although the latter are characterized by phase velocities slightly different than the fundamental IAW component, both in the hybrid-PIC and full-PIC simulations.

By contrast, in the strong drive case, the subharmonics generation gives rise to important additional ion kinetic effects, namely, a strong diffusion in phase space and a tail formation in the distribution function. The snapshots of the electron and ion phase spaces are shown in Figs. 11–13. In
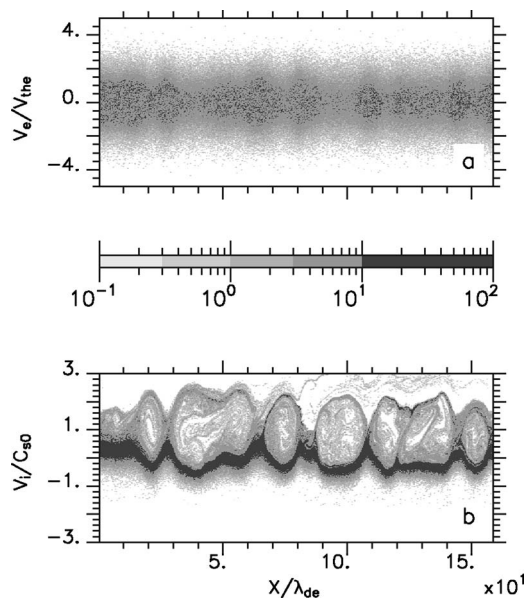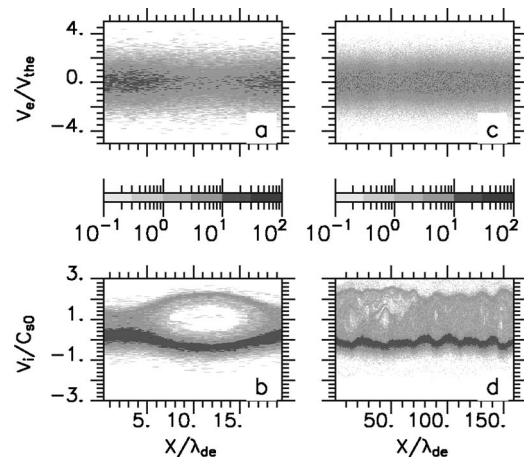

FIG. 12. Electron phase space (a) and ion phase space (b) at $\omega_{pi}t$=500, for the same parameters as in Fig. 4 (strong drive), box length is $8\lambda_m$.

order to isolate the effects associated with the subharmonics generation we compare the results of a periodic simulation carried out in a short simulation box of the length λ_m, for which the parametric decay is quenched, with those obtained with a long simulation box, $8\lambda_m$, for which harmonics generation can take place. The results corresponding to initial and late times are presented in Figs. 11 and 13. The results corresponding to the intermediate time $\omega_{pi}t$=500 are displayed in Fig. 12 for the long box only because there are no significant differences for the short box.

Figure 11 shows a snapshot of electron and ion phase spaces at the early time $\omega_{pi}t$=200. For both simulations one can see a strong ion trapping at wave amplitudes which are above the wave-breaking limit. Spatial periodic modulations can also be observed in the electron phase space. For later times, the simulations carried out in the short simulation box, for which the subharmonics generation is quenched, do not show any significant changes. By contrast, the simulation carried out in the long simulation box, for which the subharmonics generation is allowed, exhibits, at later times, the structures characterized by wavelengths longer than the fundamental wavelength λ_m (see Fig. 12), while the driven IAW amplitude decays to a small value. At the late time $\omega_{pi}t$ =1480, it can be seen in Fig. 13(d) that there is no well-defined wavelength in the ion phase space in the long box simulation. This fact can be merely understood as the consequence, in phase space, of the broad IAW spectrum displayed in Fig. 3. Moreover, in panel (c) one can see a strong diffusion in the ion velocity space, in the velocity range $[0,2]\,c_{s0}$. The phase spaces shown in panels (a) and (b), corresponding to the simulations carried out in the short box, are almost identical to those of Fig. 11 for early times, and the driven IAW amplitude remains large. Thus, the comparison between panels (b) and (d) demonstrates clearly that indeed it is the subharmonics generation which gives rise to such a strong diffusion in the ion velocity space.

The ion velocity distribution functions shown in Fig. 14 demonstrate that the ion diffusion leads also to a significant ion tail formation. At the early time $\omega_{pi}t$=200, there is no significant difference between the simulations with the long
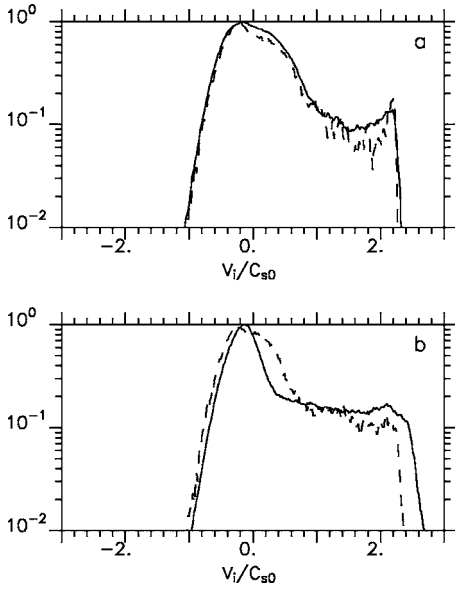
FIG. 14. Ion distribution function $f(v_i)$ for the "short'" box (dashed line), and the $8\lambda_m$ box (solid line) at $\omega_{pi}t=200$ (a) and 1480 (b) logarithmic scale. The parameters are the same as in Fig. 4 (strong drive).

FIG. 15. [Panels (a) and (b)] Average electron kinetic energy and ion kinetic energy per particle, respectively, normalized to the initial electron temperature vs time. [Panel (c)] Electrostatic energy for all modes vs time. Solid line: "short'" box (no decay) results; dotted line: $8\lambda_m$ box. Same parameters as in Fig. 4 (strong drive).

and short boxes. Both curves in panel (a) display the same features characteristic of partial particle trapping (see Ref. 33), with a small dip in the distribution function around the phase velocity $v \sim 1.6c_{s0}$, associated with a small maximum at $v \simeq 2.2c_{s0}$, corresponding therefore to a positive slope in the velocity range $[1.6, 2.2]c_{s0}$. By contrast, one can see at the late time $\omega_{pi}t=1480$ [panel (b)] that the distribution function has changed for the long simulation box. The maximum at $v \simeq 2.2c_{s0}$ is not as pronounced as in the early times; instead, the distribution function shows a slow and regular decrease in the velocity range $[0.8, 2.2]c_{s0}$. It can also be seen that the thermal part of $f_i(v)$ is partially depleted as compared with the early time $\omega_{pi}t=200$, indicating a significant diffusion from the thermal part to the hot tail. Such an ion tail is expected to result in an efficient IAW damping.

B. Particle heating and IAW damping

We have seen that subharmonics generation gives rise to a broad wave spectrum and to an additional diffusion in the ion velocity space. These features are significantly different from those characteristics of the partial ion trapping in a monochromatic wave. At the same time, the simulations show that the ion and electron kinetic energies increase. Therefore it is a relevant question whether this increase of kinetic energies is associated, or not, with a damping of the driven IAW. A wave damping is an irreversible process associated with a real *heating*, either of the bulk of the distribution function or of its tail. By contrast, the so-called *sloshing* motion of the particles in the wave corresponds to the reversible process associated with the dressing of the pure electrostatic energy of the IAW by the kinetic energy of the particles. In this subsection, we show, by estimating the ion and electron motions, that the electron heating is negligible, whereas the ion thermal energy increases substantially.
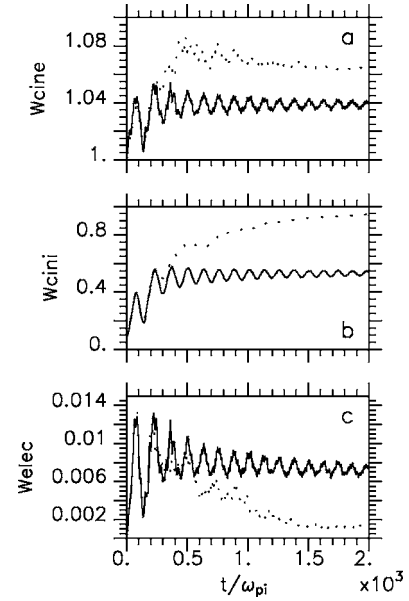
Let us estimate the particle heating by subtracting the particle sloshing energy from the whole kinetic particle energy. We recall that the energy associated with a spectrum of IAWs is given as a sum over the wave numbers:

$$\bar{W} = \frac{W}{n_{e0}T_e} = \sum_k \overline{|\phi_k|}^2 k^2 \lambda_{\text{De}}^2 \partial_\omega(\omega\epsilon)_{\epsilon=0}, \tag{8}$$

where $\epsilon = 1 + \chi_e + \chi_i$ is the real part of the dielectric function, and $\chi_e = (k\lambda_{\text{De}})^{-2}$ and $\chi_i = -(\omega^2/\omega_{pi}^2)(1+3k^2v_{\text{thi}}^2/\omega^2)$ are the electron and ion susceptibilities, respectively. In Eq. (8) we can identify three terms, $\bar{W} = \bar{W}_{\text{elec}} + \bar{W}_{\text{slosh},e} + \bar{W}_{\text{slosh},i}$. The first one, $\bar{W}_{\text{elec}} = \Sigma_k \overline{|\phi_k|}^2 k^2 \lambda_{\text{De}}^2$, corresponds to the normalized electrostatic energy of the IAWs; the second one, $\bar{W}_{\text{slosh},e} = \Sigma_k \overline{|\phi_k|}^2$, is the electron sloshing energy associated with the IAWs; the third one, $\bar{W}_{\text{slosh},i} = \Sigma_k \overline{|\phi_k|}^2 k^2 c_{s0}^2/\omega_k^2$, is the ion sloshing energy. The first term can also be written as $W_{\text{elec}} = (\epsilon_0/2)\int dx E^2$, with $E = -\partial_x \varphi$. In the simulations $k_m^2 \lambda_{\text{De}}^2 = 0.1$, therefore the first term is much smaller than the two other ones, $\bar{W}_{\text{slosh},e} \sim \bar{W}_{\text{slosh},i} \sim 10\bar{W}_{\text{elec}}$.

The average kinetic energy of each particle species was calculated from the PIC code data by summing up the kinetic energies of all particles and by dividing them by the total number of particles. According to the normalization in Eq. (8), the initial kinetic energies are $\bar{W}_{\text{cin},e}(0)=1$ and $\bar{W}_{\text{cin},i}(0) = T_i/ZT_e$. We define then the particle thermal energy as a difference between the kinetic energy and the sloshing energy, namely, $W_{\text{heat},e,i} = W_{\text{cin},e,i} - W_{\text{slosh},e,i}$. The $W_{\text{cin},e}$, $W_{\text{cin},i}$, and W_{elec} are plotted in function of time in Fig. 15 for the strong drive case and for the full-PIC simulations. The results obtained from the simulations carried out in the short and long boxes become significantly different at time $\omega_{pi}t \simeq 500$, which is the time when the subharmonics are gener-

ated (see Fig. 6). At this time, the electrostatic energy W_{elec} starts decreasing in the long box simulation. The maximum level of the electrostatic energy is $\bar{W}_{elec} \sim 0.01$, indicating that the relative level of the sloshing energy does not exceed 10%.

The most important observation which follows from Fig. 15 is that the ion kinetic energy $W_{cin,i}$ increases by almost a factor of 10: from $T_i/ZT_e = 0.09$ at the initial time to $\bar{W}_{cin,i} \simeq 0.88$ at the final time $\omega_{pi}t = 2000$ for the simulations carried out in the long box. In the case of the short box, the increase of the ion kinetic energy is twice less, $\bar{W}_{cin,i} \simeq 0.55$ at the final time. By subtracting the ion sloshing energy, we find that the ion thermal energy $\bar{W}_{heat,i}$ increases to about 0.8 in the long box simulation, while it is about 0.4 for the short box simulation. In both cases the ion heating corresponds to the hot tail formation, as can be seen in Fig. 14. In the short box simulations, the ion tail appears very early, at a time of the order of the ion bounce time. It does not evolve any longer afterwards, coherently with the assumption of a reduced damping past the ion bounce time.

The electron kinetic energy is displayed in Fig. 15(a). One can observe a slight increase of $W_{cin,e}$ of the order of 6.5% for the simulations with a long box and of less than 4% for the short box. These numbers are of the order of the electron sloshing energy as explained just above. Therefore, the variations of the electron thermal energy remain small. Thus, although the electrons give rise to an IAW frequency shift as large as 25% (see Table I), they do not play any significant role in the IAW damping.

C. Decay in the "cold ion" limit

It is interesting to verify to what extent the scenario discussed in the previous sections depends on the input parameters, especially on the initial ion temperature. In a series of simulations carried out with cold ions, $T_i/ZT_e = 0.01-0.03$, very similar behaviors were observed. In these simulations, the ion Landau damping and the ion frequency shift (4) are negligibly small, whereas the wave-breaking limit (1) is relatively high, $\delta n/n_{e0}|_{WB} \sim 0.22$ for $T_i/ZT_e = 0.03$. Here, we present the results of the full-PIC simulations, in the strong drive regime, in the long simulation box, for the same physical parameters as those of Fig. 7, namely, $\phi_d = 0.1$, $k_m^2 \lambda_{De}^2 = 0.1$, and $T_i/ZT_e = 0.03$.

The ion phase space is shown in Fig. 16. During the initial phase [panel (a)] the driven IAW reaches large amplitudes, above the wave-breaking limit, although the ion kinetic effects remain weak. A significant modification of the electron distribution function (not shown here) can already be observed, because the electrons react without any delay to the large amplitude IAW. At the time $\omega_{pi}t \simeq 40$ [panel (b)], the ion wave breaking takes place. An important difference with the base line case $T_i/ZT_e = 0.09$ is that the harmonics still have significant amplitudes when wave breaking occurs. Very quickly after the onset of ion wave breaking, subharmonics are generated. Around the time of five to seven ion acoustic periods, the fundamental IAW amplitude decays to very small values, while longer-wavelength components appear, as can be seen in panel (c). At this time, the subhar-
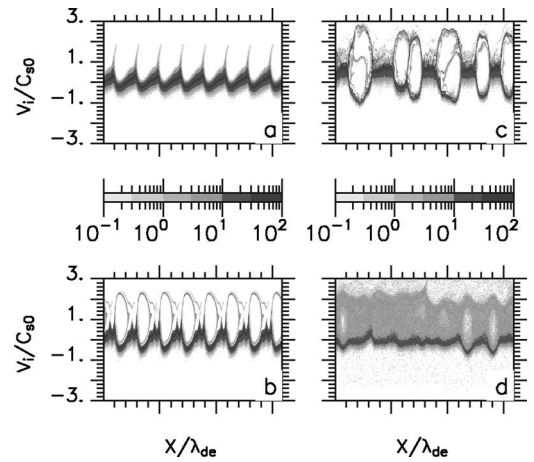

FIG. 16. Ion phase space at times $\omega_{pi}t = 20$ (a), 50 (b), 140 (c), 1500 (d). The parameters are the same as in Fig. 7 (strong drive).

monics energy content lies essentially in the half harmonic, as can be seen in the ion phase space, where the wavelength (period) doubling is clearly observed. Then, further long-wavelength modes appear, and the scenario becomes very similar to the one previously discussed in the case of a larger ion-to-electron temperature ratio. In particular, a strong diffusion can be seen in the ion velocity space at the end of simulation.

D. Sensitivity with regard to the simulation parameters

We carried out many additional simulations with the hybrid-PIC code in order to test the sensitivity of the results on the simulation box length and on the boundary conditions. To do so, we first verified that the results are not changed significantly for the box lengths of 8, 16, and $32\lambda_m$. Then, we carried out simulations with a driver localized over the length of 8 or $16\lambda_m$ within a longer simulation box of total length of $72\lambda_m$, using boundary conditions such that the outgoing particles are replaced by thermal ones. We observed similar results, with the subharmonics decay together with the temporal decrease of the driven IAW amplitude. Therefore, we consider that the periodic simulations in a simulation box of at least eight IAW lengths give reliable results applicable to larger systems.

VII. CONCLUSIONS AND DISCUSSION

The main conclusions we may draw from our studies of the nonlinear saturation of a resonantly driven IAW is that the electron kinetic effects become important whenever the nonlinear effects come into play. Therefore, the validity domain of the hybrid-PIC simulations is limited to very small IAW amplitudes. Although the electrons do not interact directly with the IAWs and do not absorb a significant part of the wave energy, the sloshing electron motion in the IAW electrostatic field leads to a flattening of the electron distribution function and, consequently, to a significant change of the IAW dispersion. We find that for large enough driving amplitudes, the electron distribution can be approximated by a hyper-Gaussian function. The fluid-type description of

IAWs in which the kinetic effects are modeled by a nonlinear frequency shift depending on the square root of the wave amplitude is limited to small IAW amplitudes and to the initial stage of the IAW evolution.

Our simulations confirm the earlier results,[6,10] showing that the electron kinetic effects favor the decay of IAWs into subharmonics. This parametric instability broadens the IAW spectrum and provokes an efficient ion diffusion in velocity space and a strong ion heating. It is not appropriate to take the wave breaking as a maximum or saturation limit in the IAW amplitude for a driven system. The excited wave can easily exceed this limit, although only for a short time, and it eventually evolves towards much smaller amplitudes and to a broad spectrum. This fact is potentially of importance in the nonlinear evolution of SBS and could help in the explanation of the low-level saturation of the SBS reflectivity observed in some cases.[19–21]

The results found in the present paper are limited to the cases where collisions could be neglected. In fact, the ion and electron collisions could restore the distribution functions back to equilibrium if the collision frequency is larger than the corresponding bounce frequency.[28] In this case, the hybrid-PIC description could be appropriate. We are currently examining the role of interparticle collisions in order to define the limits of the hybrid-PIC model.

Our results are also limited to one spatial dimension. A second dimension would enlarge the parameter space where the IAW decay instability is allowed[25] and enhance the ion diffusion in the phase space.[33] Moreover it would make it possible to take into account the effect of transverse losses.[11,13,34] Obviously, detailed comparisons are still needed with two-dimensional hybrid and PIC codes.

ACKNOWLEDGMENTS

[1] S. J. Karttunen, J. N. McMullin, and A. A. Offenberger, Phys. Fluids **24**, 447 (1981).
[2] J. A. Heikkinen, S. J. Karttunen, and R. R. E. Salomaa, Phys. Fluids **27**, 707 (1983).
[3] M. Casanova, G. Laval, R. Pellat, and D. Pesme, Phys. Rev. Lett. **54**, 2230 (1985).
[4] W. Rozmus, M. Casanova, D. Pesme, A. Héron, and J.-C. Adam, Phys. Fluids B **4**, 576 (1992).
[5] A. V. Maximov, W. Rozmus, V. T. Tikhonchuk, D. F. DuBois, H. A. Rose, and A. M. Rubenchik, Phys. Plasmas **3**, 1689 (1996).
[6] B. I. Cohen, B. F. Lasinski, A. B. Langdon, and E. A. Williams, Phys. Plasmas **4**, 956 (1997).
[7] H. X. Vu, Phys. Plasmas **4**, 1841 (1997).
[8] H. A. Rose, Phys. Plasmas **4**, 437 (1997).
[9] B. B. Afeyan, A. E. Chou, J. P. Matte, R. P. J. Town, and W. L. Kruer, Phys. Rev. Lett. **80**, 2322 (1998).
[10] B. I. Cohen, B. F. Lasinski, A. B. Langdon, E. A. Williams, H. A. Baldis, and C. Labaune, Phys. Plasmas **5**, 3402 (1998).
[11] H. X. Vu, D. F. Dubois, and B. Bezzerides, Phys. Rev. Lett. **86**, 4306 (2001); Phys. Plasmas **9**, 1745 (2002).
[12] D. Pesme, S. Hüller, J. Myatt, C. Riconda, A. Maximov, V. T. Tikhonchuk, C. Labaune, J. Fuchs, S. Depierreux, and H. A. Baldis, Plasma Phys. Controlled Fusion **44**, B53 (2002).
[13] L. Divol, B. I. Cohen, E. A. Williams, A. B. Langdon, and B. F. Lasinski, Phys. Plasmas **10**, 3728 (2003).
[14] E. A. Williams, B. I. Cohen, L. Divol, M. R. Dorr, J. A. Hittinger, D. E. Hinkel, A. B. Langdon, R. K. Kirkwood, D. H. Froula, and S. H. Glenzer, Phys. Plasmas **11**, 231 (2004).
[15] W. L. Kruer, *The Physics of Laser Plasma Interaction* (Addison-Wesley, New York, 1988).
[16] G. J. Morales and T. M. O'Neil, Phys. Rev. Lett. **28**, 417 (1972).
[17] A. A. Andreev and V. T. Tikhonchuk, Sov. Phys. JETP **68**, 1135 (1989).
[18] L. Divol, R. L. Berger, B. I. Cohen, E. A. Williams, A. B. Langdon, B. F. Lasinski, D. H. Froula, and S. H. Glenzer, Phys. Plasmas **10**, 1822 (2003).
[19] M. J. Herbst, C. E. Clayton, and F. C. Chen, Phys. Rev. Lett. **43**, 1591 (1979).
[20] C. E. Clayton, C. Joshi, and F. C. Chen, Phys. Rev. Lett. **51**, 1656 (1983).
[21] J. Handke, S. A. H. Rizvi, and B. Kronast, Phys. Rev. Lett. **51**, 1660 (1983).
[22] D. H. Froula, L. Divol, and S. H. Glenzer, Phys. Rev. Lett. **88**, 105003 (2002); D. H. Froula, L. Divol, H. A. Baldis, R. L. Berger, D. G. Braun, B. I. Cohen, R. P. Johnson, D. S. Montgomery, E. A. Williams, and S. H. Glenzer, Phys. Plasmas **9**, 4709 (2002).
[23] H. C. Bandulet, C. Labaune, K. Lewis, and S. Depierreux, Phys. Rev. Lett. **93**, 035002 (2004).
[24] C. Niemann, S. H. Glenzer, J. Knight, L. Divol, E. A. Williams, G. Gregori, B. I. Cohen, C. Constantin, D. H. Froula, D. S. Montgomery, and R. P. Johnson, Phys. Rev. Lett. **93**, 045004 (2004).
[25] C. Riconda, A. Héron, D. Pesme, S. Hüller, V. T. Tikhonchuk, and F. Detering, Phys. Rev. Lett. **94**, 055003 (2005).
[26] C. Riconda, S. Hüller, J. Myatt, and D. Pesme, Phys. Scr., T **T84**, 217 (2000).
[27] S. Hüller, Phys. Fluids B **3**, 3317 (1991).
[28] P. W. Rambo, S. C. Wilks, and W. L. Kruer, Phys. Rev. Lett. **79**, 83 (1997).
[29] H. X. Vu, D. F. Dubois, and B. Bezzerides, J. Comput. Phys. **144**, 257 (1998).
[30] J. C. Adam, A. Gourdin-Serveniere, and A. B. Langdon, J. Comput. Phys. **47**, 299 (1982).
[31] R. L. Dewar, W. L. Kruer, and W. M. Manheimer, Phys. Rev. Lett. **28**, 215 (1972).
[32] D. Pesme, C. Riconda, and V. T. Tikhonchuk, Phys. Plasmas **12**, 092101 (2005).
[33] B. I. Cohen, L. Divol, A. B. Langdon, and E. A. Williams, Phys. Plasmas **12**, 052703 (2005).
[34] H. A. Rose and D. A. Russel, Phys. Plasmas **8**, 4784 (2001).